Article

Semi-Analytical Retrieval of the Diffuse Attenuation Coefficient in Large and Shallow Lakes from GOCI, a High Temporal-Resolution Satellite

Changchun Huang [1,2,3,4] (ID) **and Ling Yao** [5,*] (ID)

1   School of Geography Science, Nanjing Normal University, Nanjing 210023, China; huangchangchun@njnu.edu.cn
2   State Key Laboratory of Lake Science and Environment, Nanjing Institute of Geography and Limnology, Chinese Academy of Sciences, Nanjing 210023, China
3   Key Laboratory of Virtual Geographic Environment (Nanjing Normal University), Ministry of Education, Nanjing 210023, China
4   Jiangsu Center for Collaborative Innovation in Geographical Information Resource Development and Application, Nanjing Normal University, Nanjing 210023, China
5   State Key Laboratory of Resources and Environmental Information System, Institute of Geographic Sciences and Natural Resources Research, Chinese Academy of Sciences, Beijing 100101, China
*   Correspondence: yaoling@lreis.ac.cn; Tel.: +86-10-6488-9045

Abstract: Monitoring the dynamic characteristics of the diffuse attenuation coefficient ($K_d(490)$) on the basis of the high temporal-resolution satellite data is critical for regulating the ecological environment of lake. By measuring the in-situ $K_d(490)$ and the remote-sensing reflectance, a semi-analytical algorithm for $K_d(490)$ was developed to determine the short-term variation of $K_d(490)$. From 2006 to 2014, the data about 412 samples (among which 60 were used as match-up points, 282 for calibrating dataset and the remaining 70 for validating dataset) were gathered from nine expeditions to calibrate and validate the aforesaid semi-analytical algorithm. The root mean square percentage error (RMSP) and the mean absolute relative error (MAPE) of validation datasets were respectively 27.44% and $22.60 \pm 15.57\%$, while that of the match-up datasets were respectively 34.29% and $27.57 \pm 20.56\%$. These percentages indicate that the semi-analytical algorithm and Geostationary Ocean Color Imager (GOCI) data are applicable to obtain the short-term variation of $K_d(490)$ in the turbid shallow inland waters. The short-term GOCI-observed $K_d(490)$ shows a significant seasonal and spatial variation and a similar distribution to the matching Moderate Resolution Imaging Spectroradiometer (MODIS) which derived $K_d(490)$. A comparative analysis on wind (observed by buoys) and GOCI-derived $K_d(490)$ suggests that wind is a primary driving factor of $K_d(490)$ variation, but the lacustrine morphometry affects the wind force that is contributing to $K_d(490)$ variation.

Keywords: Geostationary Ocean Color Imager (GOCI); Lake Taihu; semi-analytical algorithm; wind speed

1. Introduction

The diffuse attenuation coefficient (K_d) is a fundamental optical property that describes the transfer process of light and heat in the aquatic ecosystems [1]. It is a better estimator of the euphotic depth and light availability in various depths compared with the traditional method using secchi disk. K_d is affected by the water constituents, the inherent optical properties, the incident light angle and etc., and thus obviously possesses the quasi-optical properties [2–4]. Therefore, the spatial and temporal variation of K_d is significant since it could indicate the dynamic changes in these represented factors [5,6]. The accurate estimation of K_d and its distribution is critical for understanding

and modeling the biochemical and physical processes, such as photobleaching, phytoplankton photosynthesis and organism mineralization in the euphotic zone of the aquatic ecosystems [7,8].

Satellite remote sensing could promptly provide the repeated synoptic information on K_d [9–11] and several empirical algorithms for K_d at the wavelength of 490 nm ($K_d(490)$), which have been developed to estimate $K_d(490)$ in clear waters [7,12,13]. In order to accurately determine K_d or $K_d(490)$, Lee et al. [3] proposed a semi-analytical algorithm based on radiation transfer simulation. After that, Wang et al. [9] improved such semi-analytical algorithm because of its inability to predict backscatter coefficient (b_b) (estimation uncertainty > 50%) in highly turbid coastal waters [14,15]. The improved semi-analytical algorithm could retrieve K_d and $K_d(490)$ with a relatively acceptable accuracy in optically complex coastal waters [9,11,15]. Therefore, K_d and $K_d(490)$ have become the important optical parameters for ocean satellite imagers, such as Moderate Resolution Imaging Spectroradiometer (MODIS), Sea-Viewing Wide Field-of-View Sensor (SeaWiFS), MEdium Resolution Imaging Spectrometer (MERIS) and Geostationary Ocean Color Imager (GOCI) [10,16–18], and are processed by the empirical or semi-analytical algorithms.

The empirical algorithms have also been used to estimate $K_d(490)$ and the diffuse attenuation coefficient of the photosynthetically active radiation ($K_d(PAR)$) in the extremely turbid and productive inland lakes [5,7,17]. However, the application of the semi-analytical algorithms for K_d and $K_d(490)$ in the turbid inland lakes (such as Lake Taihu, the third largest freshwater lake in China) is seldom reported, which is primarily due to the following reasons: (1) in order to provide the accurate semi-analytical estimation of K_d, the absorption (a) and b_b must be derived precisely first [3]; (2) whether the quasi-analytical algorithm (QAA) [19] or b_b has been first derived or not [9,20], the validated relationship between the remote-sensing reflectance (R_{rs}) and a (or b_b) is the foremost; and it's difficult to accurately measure the inherent optical properties, especially b_b, in the highly turbid inland waters [21].

Based on satellite data, the long-term records of K_d in lakes have revealed the large temporal and spatial variation of K_d caused by the meteorological and geographical features of lakes [5,6,17]. To reflect the significant short-term spatial and temporal variation of K_d, a high temporal-resolution satellite is required to characterize the dynamic features of K_d [10,11], which is particularly necessary for the shallow inland lakes having high dynamic ratio ((square root of the area)/depth), such as Lake Taihu with a dynamic ratio of 25.4. In conclusion, the semi-analytical algorithm of K_d applied in GOCI satellite is important and critical to the observation of K_d in the shallow inland lakes.

The objectives of this study were (1) to develop a semi-analytical algorithm of K_d for the GOCI sensor based on $K_d(490)$ and R_{rs} measured in situ, (2) to reveal the necessity of tracing the high temporal-resolution fluctuations in $K_d(490)$, and (3) to monitor the highly dynamic characteristics of $K_d(490)$ by using GOCI-derived results.

2. Materials and Methods

2.1. In-Situ Measurement

2.1.1. Study Area

Located in the Yangtze River delta, Lake Taihu is a large shallow eutrophic lake with a surface area of 2338 km^2 and a mean depth of 1.9 m [7]. In Lake Taihu, the sediment resuspension frequently occurs due to its high lacustrine dynamic ratio and the East Asian monsoon. Most water area of Lake Taihu is extremely turbid where $K_d(490)$ can reach 20 m^{-1}. However, East Lake and East Bay (see its aquatic plant in Figure 1) are very clear and contain a large amount of the submerged aquatic vegetation.

From 2006 to 2014, the remote-sensing reflectance (R_{rs}) and the ambient downwelling irradiance (E_d) were measured in situ by taking 473 samples in nine expeditions (respectively in November 2006, November 2007, November 2008, April 2009, May 2010, August 2011, October 2012, August 2013 and October 2014). During the in-situ measurement of the optical properties (R_{rs} and E_d), water samples were collected. The water quality (suspended particulate matter, SPM) was measured in the laboratory

within 24 h after water samples have been collected. In order to obtain the high-quality data about $K_d(490)$, measurements carried out under the low solar radiance conditions ($E_d(\lambda,z)/E_d(\lambda,0^+) < 1\%$) were removed. In final, we left 412 samples, among which 60 (from 6 August 2013 to 10 August 2013 marked in Figure 1) were used as match-up points (their in-situ measurement time is synchronous with the transit time of satellite images), and 282 were selected randomly to calibrate the model, while the remaining 70 were to validate the model. The wind speed and direction were observed by putting 10 buoys on the lake (see Figure 1).
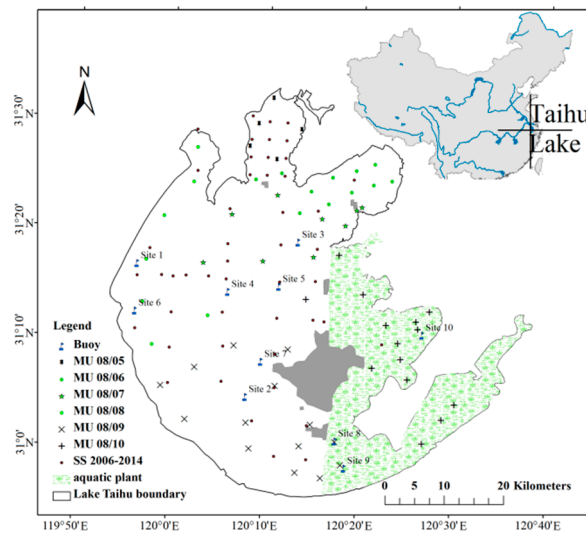

Figure 1. Sample sites of in-situ measurement. MU (match up points collected from 6 August 2013 to 10 August 2013) was marked from SS (sample sites) of the expeditions from 2006 to 2014.

2.1.2. Measurements of the Optical Properties and SPM

R_{rs} (Figure 2A) was measured by using an analytical spectral device, i.e., the FieldSpec spectroradiometer (350–1050 nm with the sampling interval of 1 nm). Each element (reference panel, water and sky) was measured after instrument optimization and calibrating for dark current. The radiances of reference panel ($L_p(\lambda,0^+)$), water ($L_{sw}(\lambda,0^+)$), sky ($L_{sky}(\lambda,0^+)$) and the panel again were measured ten times with the abnormal spectra being removed [22]. The rest of spectra were used to calculate R_{rs} according to the following formula:

$$R_{rs}(\lambda) = (L_{sw}(\lambda,0^+) - r * L_{sky}(\lambda,0^+))/(L_p(\lambda,0^+) * \pi/\rho_p(\lambda)) \tag{1}$$

where *r* refers to the air–water surface reflectance (with a value of 2.45%), and $\rho_p(\lambda)$ refers to the reflectance of the standard reflectance panel.

Downwelling irradiance ($E_d(\lambda,z)$) was measured by TriOS RAMSES-ARC (Ramses, Germany) with a spectral resolution of 3.3 nm (sampling interval of 1 nm) for each depth (from 0.2 to 1.4 m with the interval of 0.2 m). Each depth was measured for ten times with the abnormal spectra being removed, by using a method which is similar to the estimation process of R_{rs}. K_d (see Figure 2B) using a non-linear fit between $E_d(\lambda,z)$ and depth (*z*):

$$E_d(\lambda,z) = E_d(\lambda,0^-) \times \exp(-K_d(\lambda) \times z) \tag{2}$$

K_d is acceptable when R^2 of non-linear fit regressions ≥ 0.99 and the number of depths in regressions ≥ 4.
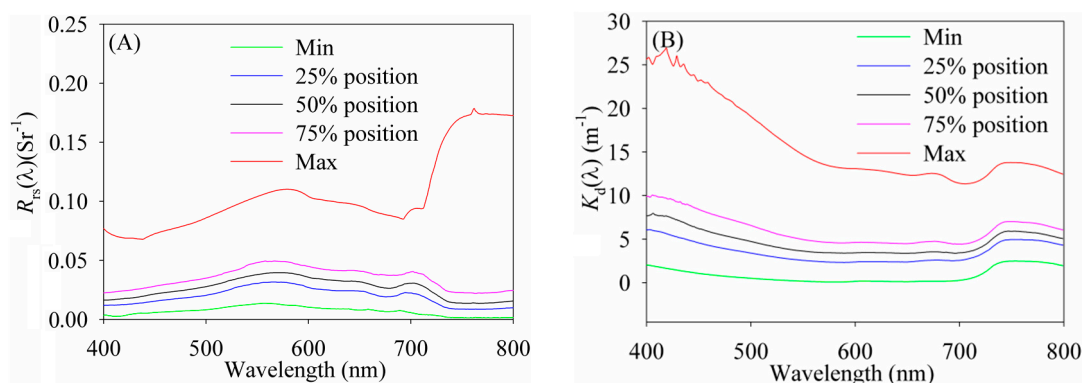
Figure 2. In-situ measurement of the remote-sensing reflectance (**A**) and the diffuse attenuation coefficient (**B**). The 25%, 50% and 75% lines respectively indicated the quarter, median and three-quarter levels of R_{rs} and K_d datasets, and Min and Max respectively refer to the minimum and maximum values of datasets.

SPM was obtained by measuring the mass differences between the pre-combusted (550 °C for 4 h) and dried (105 °C for 4 h) 07-μm Whatman GF/F glass fiber filters both before and after filtration of whole water field samples.

2.2. Satellite Data and Preprocessing

GOCI is the first geostationary ocean-color satellite sensor, with the spatial resolution of 500 m and the temporal resolution for one hour (eight times per day, i.e., from local time 8:30 to 15:30). The matching GOCI images (level-1b, from 8 June 2013 to 8 September 2013) were downloaded from Korea Ocean Satellite Center (http://kosc.kiost.ac/eng/). The data and processes of geometry and atmosphere corrections were the same as the study of Huang et al. [23].

MODIS images from 8 June 2013 to 8 September 2013 were downloaded from the US NASA Goddard Space Flight Center (GSFC, http://oceancolor.gsfc.nasa.gov). The radiometric and geometric correction of the acquired MODIS Aqua Level 0 data was processed by SeaDAS 6.4. The parameters (satellite angle information, ozone and water vapor) from SeaDAS 6.4 were used as the input parameters in the atmospheric correction. The land target-based atmospheric correction method [24,25] was selected to derive reflectance from the MODIS-Aqua data over Lake Taihu.

2.3. Accuracy Assessment

The root mean square percentage error (RMSP) and the mean absolute relative error (MAPE) were used to assess accuracy of the model performance:

$$\text{MAPE} = \sum \left| \frac{K_{\text{estimated}} - K_{\text{measured}}}{K_{\text{measured}}} \right| / N \times 100\% \tag{3a}$$

$$\text{RMSP} = \sqrt{\sum_{i=1}^{n} \left(\frac{K_{\text{estimated}} - K_{\text{measured}}}{K_{\text{measured}}} \right)^2 / N} \times 100\% \tag{3b}$$

3. Model K_d(490)

3.1. Calibration

The relationship between K_d and the inherent optical properties (*a* and b_b) was used by Lee et al., to estimate K_d semi-analytically [3]:

$$K_d(\lambda_0) = m_0 a(\lambda_0) + m_1 (1 - m_2 \exp(-m_3 a(\lambda_0))) b_b(\lambda_0) \tag{4a}$$

The four model parameters (m_0, m_1, m_2 and m_3) were estimated by curve fitting from the simulated data of radiation transfer (values of m_0, m_1, m_2 and m_3 are listed in [3]). At first, in order for the accurate estimation of $K_d(\lambda_0)$, the inherent optical properties ($a(\lambda_0)$ and $b_b(\lambda_0)$) should be derived precisely by Equation (4a). According to Doron et al. [20] and Wang et al. [9], an empirical relationship between $b_b(\lambda_0)$ and R_{rs} based on red wavelength in turbid water (Equation (4b)) was established. However, due to the uncertainty in measurement of b_b in the highly turbid inland waters [21], the model parameters (A_0 and A_1) are hard to estimate via the in-situ measurement of $b_b(\lambda_0)$ and R_{rs}. Thus, this relationship was used to model $K_d(\lambda_0)$ combined with Equation (4a–e).

$$\ln(b_{bp}(\lambda_0)) = A_0 \times \ln(\frac{R_{rs}(\lambda_i)}{R_{rs}(\lambda_j)}) + A_1 \tag{4b}$$

$$a(\lambda_0) = \frac{(1 - U(\lambda_0))}{U(\lambda_0)} b_b(\lambda_0) \tag{4c}$$

$$U(\lambda_0) = \frac{b_b(\lambda_0)}{a(\lambda_0) + b_b(\lambda_0)} = \frac{-0.084 + (0.084 + 4 \times 0.17 \times r_{rs}(\lambda_0))^{1/2}}{2 \times 0.17} \tag{4d}$$

$$R_{rs}(\lambda_0) = 0.52 r_{rs}(\lambda_0) / (1 - 1.7 r_{rs}(\lambda_0)) \tag{4e}$$

where $r_{rs}(\lambda)$ refers to the remote-sensing reflectance just beneath the water surface and $U(\lambda)$ refers to the intermediate variable. The modeled $K_d(\lambda_0)$ (noted as $K_d(\lambda_0)_{\text{modeled}}$) and the in-situ measured $K_d(\lambda_0)$ (noted as $K_d(\lambda_0)_{\text{measured}}$) were used to estimate A_0 and A_1 via the optimal computation according to the following objective equation:

$$F_{\text{obj}} = -\sqrt{\sum_{i=1}^{n} (K_d(\lambda_0)_{\text{measured}} - K_d(\lambda_0)_{\text{modeled}})^2 / n} \tag{5}$$

Finally, the model parameters (A_0 and A_1) and the optimal bands (λ_j and λ_j in Equation (2)) were obtained when F_{obj} met the minimum value.

Three bands (λ_0, λ_i and λ_j) are necessary in this semi-analytical model. However, due to the ambiguous extrapolation index of the aerosol model [6,9,26], it's very difficult to accurately estimate R_{rs} from satellite images at short wavelengths (such as $R_{rs}(490)$) in the highly turbid inland water. There are two methods which can be used to deal with such problem. One is to calculate $R_{rs}(490)$ by taking use of the satellite-derived $R_{rs}(\lambda_0)$ and its in-situ relationship with $R_{rs}(490)$. The other is to firstly estimate $K_d(\lambda_0)$ when $R_{rs}(\lambda_0)$ can be derived well, and then calculate $K_d(490)$ by taking use of the in-situ relationship between $K_d(490)$ and $K_d(\lambda_0)$. The comparison of relationship between $K_d(\lambda)$ and $R_{rs}(\lambda)$ suggests that the relationship between $K_d(490)$ and $K_d(\lambda_0)$ (see Figure 3A) is much stronger than the relationship between $R_{rs}(490)$ and $R_{rs}(\lambda_0)$ (see Figure 3B). Thus, we chose to estimate $K_d(490)$ by retrieving $K_d(\lambda_0)$.

The calibration dataset, with $K_d(490)$ ranging from 1.82 to 19.45 m^{-1}, was used to calibrate the semi-analytical model of $K_d(490)$. The optimal band ratio in Equation (4b) was confirmed as $R_{rs}(660)/R_{rs}(555)$ via the iterative computation of $R_{rs}(\lambda_i)$ and $R_{rs}(\lambda_j)$ within the range of the GOCI band (λ_0 was set as 660 nm). Consequently, two bands ($R_{rs}(660)$, $R_{rs}(660)/R_{rs}(555)$) were used to estimate $K_d(660)$ from which $K_d(490)$ can be calculated. The optimal model parameters of A_0 and A_1 are 2.7714 and 0.8134, respectively. The RMSP and MAPE between $K_d(490)_{\text{modeled}}$ and $K_d(490)_{\text{measured}}$ are respectively 24.80% and 19.38 $\pm$ 14.47% (Figure 4A). The intermediate variable and backscatter coefficient at 660 nm, $b_{bp}(660)$, are highly positively correlated to the suspended particulate matter ($b_{bp}(660) = 0.4068 * \text{SPM}^{0.3409}$, $R^2 = 0.71$) (Figure 4B). The parameters of $K_d(490)$ algorithm for MODIS were confirmed by using a method similar to the one used for GOCI [27].
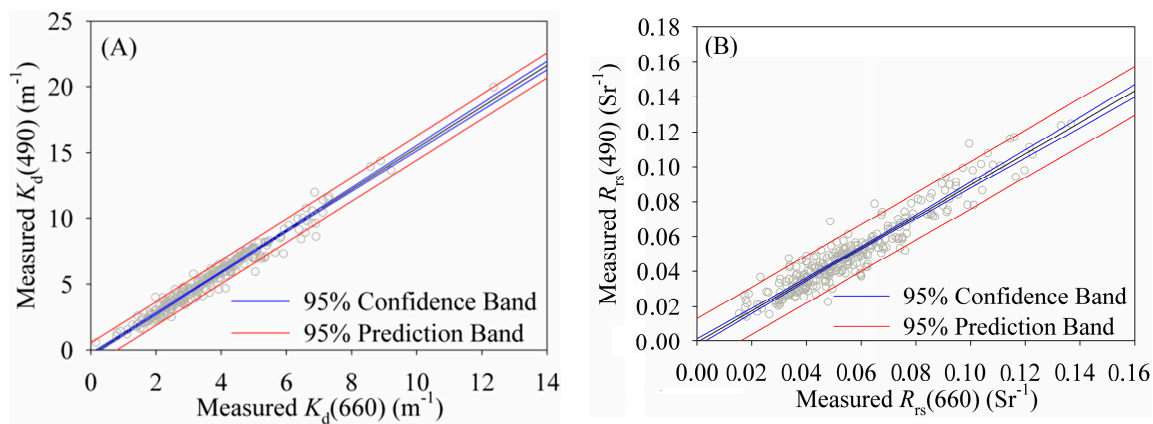
Figure 3. The in-situ relationships between $K_d(490)$ and $K_d(660)$ (**A**), and between $R_{rs}(490)$ and $R_{rs}(660)$ (**B**). The relationships are $K_d(490) = 1.5706*K_d(660) - 0.3535$, $R^2 = 0.97$ and $R_{rs}(490) = 0.8989*R_{rs}(660) - 0.0004$, $R^2 = 0.90$.
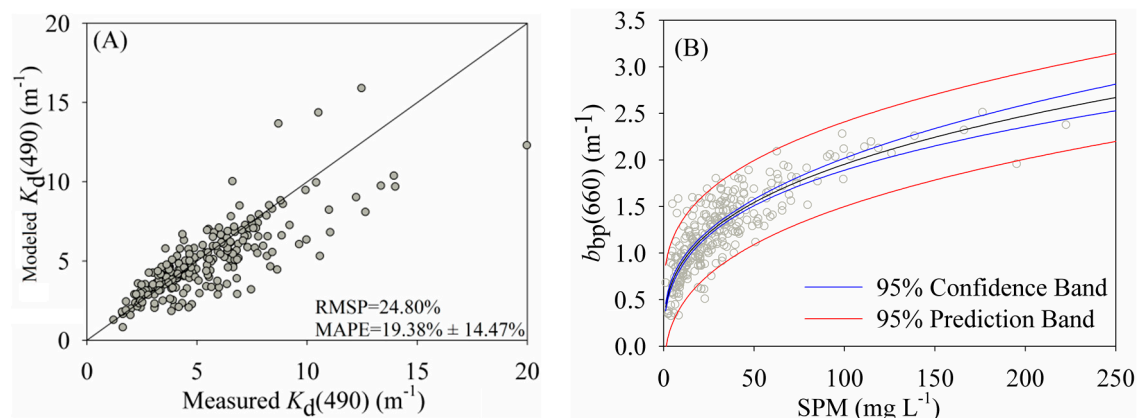

Figure 4. (**A**) Comparison of the in-situ measured $K_d(490)$ and the modeled $K_d(490)$ by using retrieval algorithm in this study. (**B**) The relationship between the estimated $b_{bp}(660)$ and the measured suspended particulate matter (SPM).

3.2. Model Validation by the In-Situ and Match-Up Measurements

The validation dataset (having 70 samples) and the match-up points (having 60 samples) were used to validate the semi-analytical algorithm of $K_d(490)$. The RMSP and MAPE of validation results between the measured and the derived $K_d(490)$ were 27.44% and 22.60 ± 15.57%, respectively (see Figure 5A). GOCI-derived $K_d(490)$ was selected from satellite images according to the latitude and longitude of the match-up points. The RMSP and MAPE of the match-up points between the measured and the derived $K_d(490)$ were respectively 34.29% and 27.57 ± 20.56% (see Figure 5B). The validation results indicated that the performance of the semi-analytical $K_d(490)$ algorithm is acceptable which can be used to estimate $K_d(490)$ from GOCI satellite images.
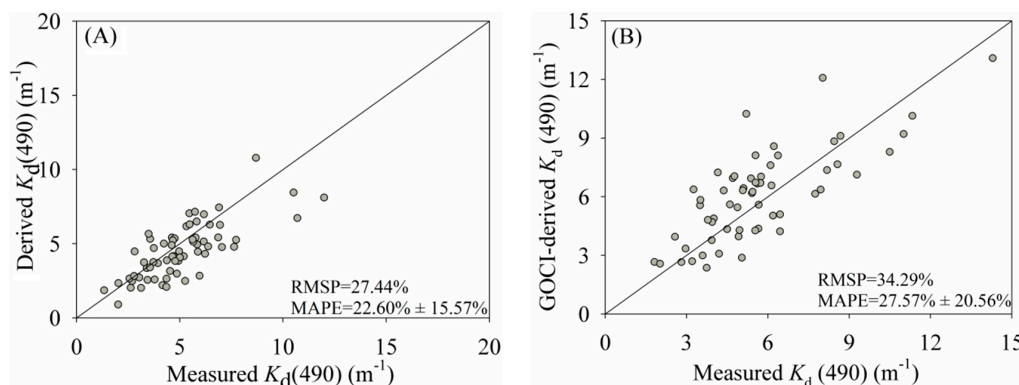
Figure 5. Comparison of the in-situ measured $K_d(490)$ and the estimated $K_d(490)$ for (**A**) validation dataset (with 70 samples) and (**B**) the match-up points (with 60 samples).

3.3. Comparison with the Exist $K_d(490)$ Model for GOCI

The previous studies proposed several semi-analytical algorithms for estimating $K_d(490)$ in the turbid water [9,11,15]. These semi-analytical algorithms were selected to compare the models (see Figure 6 and Table 1). The calibration dataset (282 points) was used to recalibrate the model parameters for Models 1, 2 and 3. Model 4 is an optimization algorithm which doesn't need calibration dataset. Thus, the validation results for Models 1, 2, 3 and 4 are getting from 70 points (validation dataset) and 372 points (validation and calibration dataset). Models 2 and 3 work well for the relatively low $K_d(490)$, but are slightly weak for the high $K_d(490)$. The performance of Model 4 in the high $K_d(490)$ is much better than Models 2 and 3, which is consistent with the previous studies in the turbid coastal water [9,11,15]. However, Model 4 will significantly overestimate $K_d(490)$ in the algal dominant water (see the red hollow circle in Figure 6), which indicates that, although the semi-analytical algorithm can be used to estimate $K_d(490)$ in the high turbid eutrophication water, but its performance is affected by the local parameters and parameterization of the inherent optical properties.
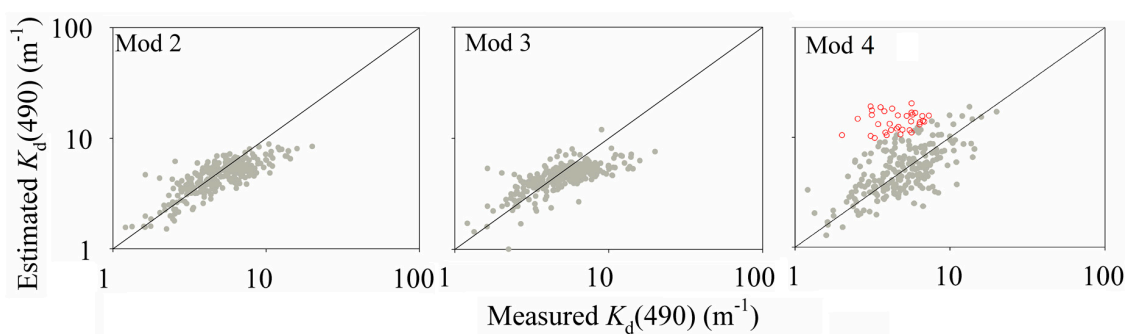

Figure 6. Comparison of the in situ measured $K_d(490)$ and the estimated $K_d(490)$ of Models 2, 3 and 4 in the model set (see Table 1), Models 2 and 3 are from Huang [27].

Table 1. Comparison of the semi-analytical model sets for $K_d(490)$. The validation results for Models 1, 2 and 3 are from validation dataset (having 70 points). Models 2 and 3 are from Huang [27]. The validation result for Model 4 is from 372 points (validation and calibration dataset) as it doesn't need calibration dataset.

Models	Variables	R^2	RMSP	$|RE|_{Max}$	MAPE
Model 1 (This study)	$R_{rs}(660)/R_{rs}(555)$	0.57	27.44%	76.11%	$22.60 \pm 15.57\%$
Model 2 [15]	$R_{rs}(667)$, $R_{rs}(490)$	0.55	29.07%	115.38%	$24.59 \pm 16.03\%$
Model 3 [9]	$R_{rs}(488)$, $R_{rs}(645)/R_{rs}(488)$	0.41	29.60%	140.09%	$24.28 \pm 18.54\%$
Model 4 [11]	(400–800 nm with 10 nm interval)	0.44	33.23%	175.27%	$31.24 \pm 24.16\%$

4. Results and Discussion

4.1. Short-Term Observation of K_d(490) from GOCI

The hourly scale maps of GOCI-derived K_d(490) in Lake Taihu were obtained by using the semi-analytical algorithm (see Figure 7). The retrieval results of K_d(490) in East Lake and East Bay (see the aquatic plant in Figure 1) were invalidated due to the effect of the submerged plants and bottom reflectance [28] and thus weren't shown in the retrieval results. The hourly scale maps of K_d(490) can show the consecutive dynamic characteristics of K_d(490) at both the spatial and the temporal scales. The high K_d(490) values were mainly distributed in the northwestern and southwestern areas of Lake Taihu as affected by sediment resuspension and algal blooms in summer [22,29]. The low K_d(490) values were distributed beyond the algal bloom area, such as the center area of the lake, where sediment resuspension is rare (8 June 2013 in Figure 7). The dynamic characteristics of K_d(490) are consistent with the diffusion and migration of algae where sediment resuspension is weak (8 June 2013 in Figure 6). Sediment resuspension significantly regulates the distribution of K_d(490) in Lake Taihu as a result of the high K_d(490) values coupled with the high wind speed, as observed on 8 August 2013 (see Figure 7). The high K_d(490) value of 8.67 m^{-1} appears when wind has reached 5.26 ± 1.88 m s^{-1} for a duration of four hours. In conclusion, both algae and sediment resuspension can impact the distribution of K_d(490) in summer, and the algae or sediment resuspension is affected by wind speed. Thus, to derive the highly dynamic characteristics of K_d(490) requires the high temporal-resolution satellite data.
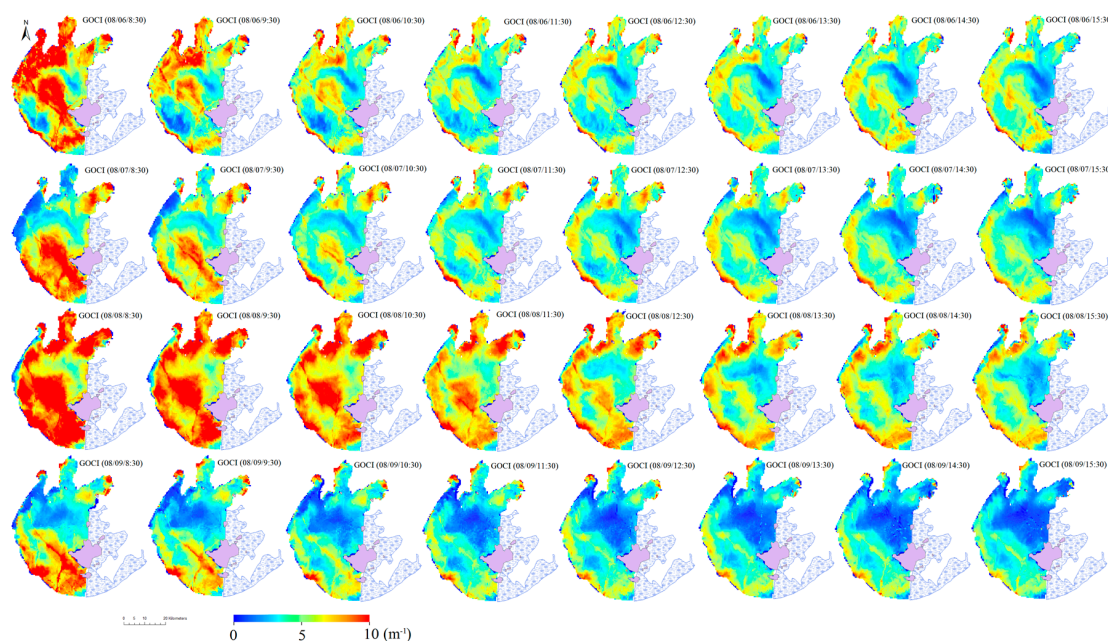

Figure 7. The spatial variations of K_d(490) mapped by GOCI data during daytime hours from August 6 to August 9. The retrieval results of K_d(490) in East Lake and East Bay (see the aquatic plant in Figure 1) are not shown.

4.2. Comparison of MODIS-Derived and GOCI-Derived K_d(490)

The transit time of MODIS satellite is similar to that of GOCI satellite; both of which pass over the territory at 13:30 (the local time). The comparison of the results retrievad from GOCI and MODIS satllite images shows that there were some inconsistencies between GOCI- and MODIS-derived K_d(490) (marked by ellipses in Figure 8). The largest inconsistence was found in the central area of Lake Taihu, which has more than 100% difference between GOCI- and MODIS-derived K_d(490) (8 June 2013 in Figure 8). Some relatively high inconsistencies were also found in the central area of the lake on 8 August 2013. The aforesaid inconsistences may be caused by the quick sediment resuspension in

the central area of the lake according to the high dynamic characteristics (see the high wind speed at sites 3, 4 and 5 in Figure 1). However, the general patterns of $K_d(490)$ distribution are consistent with each other, which indicates that models and satellite images are suitable for $K_d(490)$ estimation from MODIS and GOCI. The mean differences $((K_d(490)\text{-}_{MODIS} - K_d(490)\text{-}_{GOCI})/K_d(490)\text{-}_{GOCI})$ between GOCI- and MODIS-derived $K_d(490)$ in 8 June 2013, 8 July 2013, 8 August 2013 and 8 September 2013 are respectively $28.56 \pm 30.40\%$ (the mean value $\pm$ standard deviation), $-6.3 \pm 23.59\%$, $7.24 \pm 60.21\%$ and $-4.04 \pm 20.47\%$. The mean absolute differences (abs $((K_d(490)\text{-}_{MODIS} - K_d(490)\text{-}_{GOCI})/K_d(490)\text{-}_{GOCI}))$ are respectively $30.80 \pm 28.20\%$, $11.73 \pm 21.42\%$, $15.72 \pm 59.62\%$ and $13.53 \pm 15.88\%$.
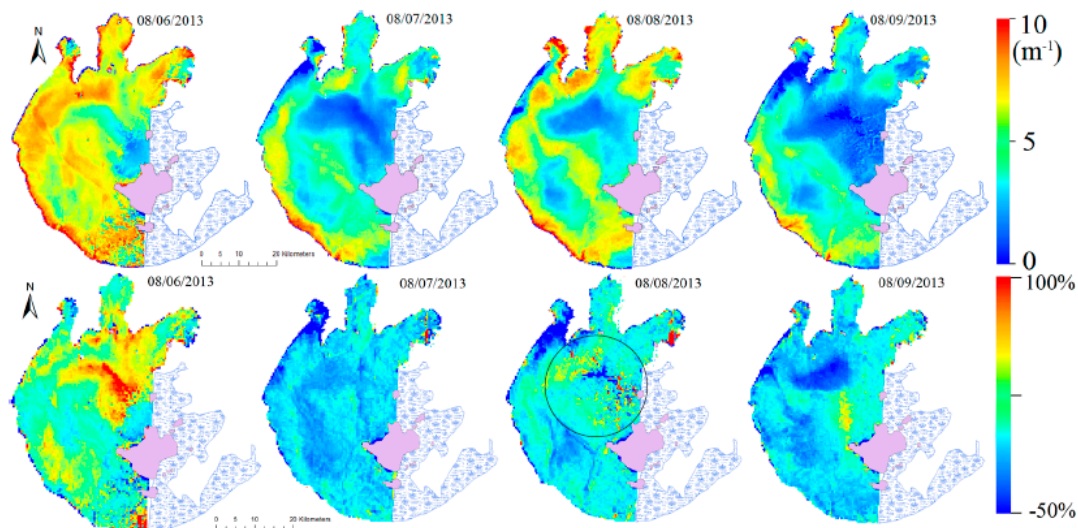

Figure 8. The above figures are the spatial variations of $K_d(490)$ mapped by MODIS data from August 6 to August 9. The figures below are the spatial differences (%) between GOCI- and MODIS-derived $K_d(490)$.

The MODIS-derived $K_d(490)$ was re-sampled to the spatial resolution of 500 m, which is same as that of GOCI. To further evaluate the consistency between GOCI- and MODIS-derived $K_d(490)$ pixel by pixel, a scatterplot of the estimated $K_d(490)$ from GOCI and MODIS data is shown in Figure 9. MODIS-derived $K_d(490)$ was slightly higher than GOCI-derived $K_d(490)$ on 8 June 2013, especially in the low value range (see Figure 9). It is clear that most of the pixels of $K_d(490)$ are consistently between the results from MODIS and GOCI (see 8 July 2013, 8 August 2013 and 8 September 2013 in Figure 9). The mean values of the linear-determined coefficient and RMSE of GOCI- and MODIS-derived $K_d(490)$ are 0.44 ± 0.13 and 1.51 ± 0.31 m^{-1}, respectively. Given the discrepancies in the satellite image process and the $K_d(490)$ algorithm and the signal/noise ratio from MODIS and GOCI, a comparison between MODIS- and GOCI-derived $K_d(490)$ indicates that the combination of MODIS and GOCI satellite data can provide the long-term observation of $K_d(490)$ with the detailed short-term dynamic information.
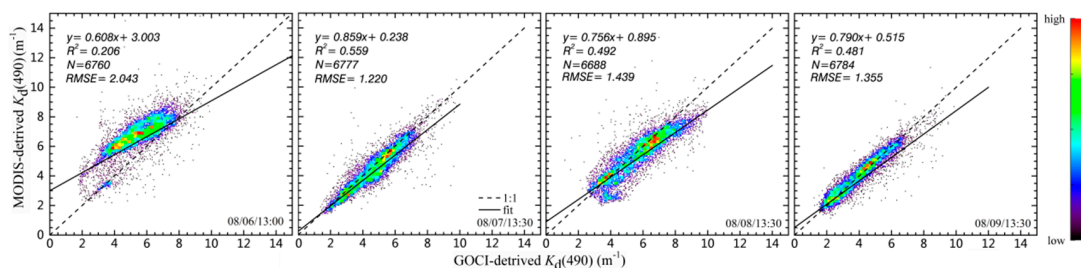

Figure 9. Comparison between GOCI- and MODIS-derived $K_d(490)$ for matching up satellite images pixel by pixel. The bad pixels were removed.

4.3. Wind-Driven Variation of K_d(490) from GOCI-Derived K_d(490)

The strength and duration of wind govern the sediment resuspension and the formation of algal blooms [29–32]. Floating algae will appear on the water surface when the wind speed is low, which would suspend on the water if the wind speed increases [23,33–35]. K_d(490) will significantly increase as a result of sediment resuspension caused by wind speed increase [36]. Consequently, wind drives the variation of K_d(490) by distributing algae and causing sediment resuspension. However, wind's regulating effect on K_d(490) also varies with spaces due to the impact of the lacustrine morphology and fetch length. The hourly values of wind speed and K_d(490) are presented in Figure 10 (the sites correspond with the buoy sample sites in Figure 1). Variations of wind speed and K_d(490) in sites 1 and 6 are clearly different from the others as K_d(490) increases with a wind speed decrease (see the black box in sites 1 and 6 of Figure 10) due to floating algae in sites 1 and 6 (algae dominant) [23]. K_d(490) also decreases with a reduction in wind speed (see the green boxes in sites 1 and 6 of Figure 10) when wind speed is higher than 5 m s^{-1}. Due to the persistent high wind speed before this period, the floating algae replaced the sediment resuspension. K_d(490) was highly and positively related to wind speed in sites 3, 4 and 5 (r = 0.5, 0.7 and 0.8 respectively), which was caused by sediment resuspension from 8 June to 8 September (sediment resuspension dominant type and floating algae are very rare). The relationships between wind speed and K_d(490) in sites 2 and 7 were not validated, which may be caused by the unstable wind directions in these two points due to the impact of land. Thus, wind drove the variation of K_d(490) but were affected by the lacustrine morphology and wind directions.
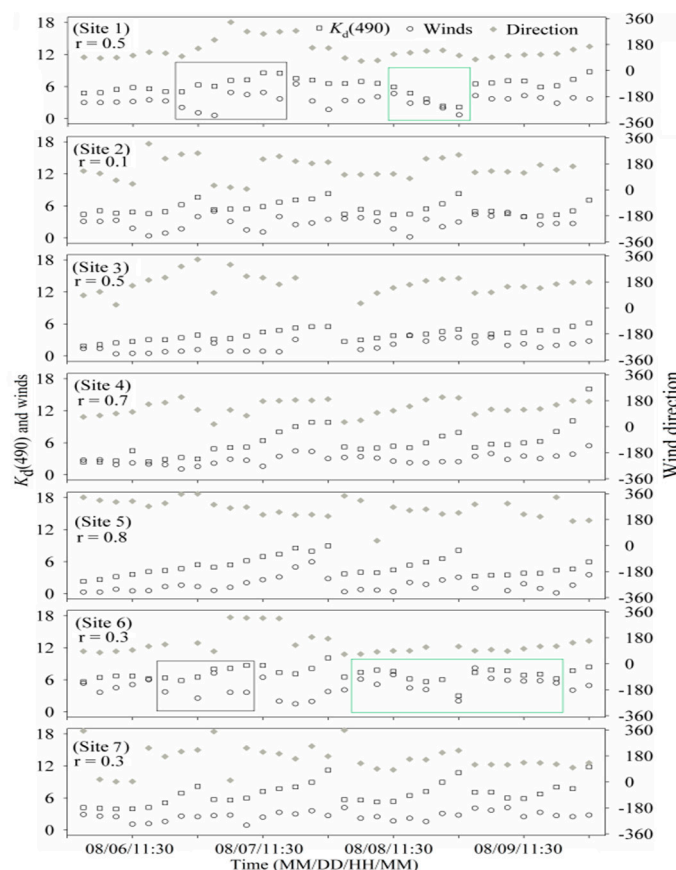

Figure 10. The hourly variation of GOCI-derived K_d(490) with wind speeds and directions for different buoy monitor sites.

To further reveal the relationship between wind speed and K_d(490), K_d(490) was divided into three types according to the strength of wind (0–3 m s^{-1}, 3–4 m s^{-1} and >4 m s^{-1}), corresponding to

the critical wind speeds of algal blooms and sediment resuspension [23,33]. When the wind speed was less than 3 m s^{-1}, $K_d(490)$ varied from 1.87 m^{-1} to 11.22 m^{-1} with a mean value of 4.92 $\pm$ 1.71 m^{-1}. Such wind speed can explain 19.14% of the variation of $K_d(490)$ due to the dominant effect of algal blooms (linear R^2 = 0.19, *p* < 0.0001). When the wind speed was less than 3 m s^{-1}, $K_d(490)$ ranged from 3.84 to 10.78 m^{-1} with a mean value of 6.47 $\pm$ 1.67 m^{-1}, and the relationship between the wind speed and $K_d(490)$ was relatively weak (linear R^2 = 0.02, *p* < 0.28). When the wind speed was less than 3 m s^{-1}, $K_d(490)$ ranged from 4.51 to 10.37 m^{-1} with a mean value of 6.95 $\pm$ 1.22 m^{-1}. Such wind speed can explain 35.57% of the variation of $K_d(490)$ due to sediment resuspension, and the ratio of which would increase to 59.58% when the black point in Figure 11 has been removed. The regression formula for wind speed (*W*) and $K_d(490)$ at the lowest value of each wind speed range (see the floor level of Figure 11) is $K_d(490)$ = 2.293 + 0.466*(exp (0.160**W*) − 1)/0.160 (R^2 = 0.89, *p* < 0.0001, N = 64), which may be caused by the relationship between wind speed (*W*) and $K_d(490)$ due to sediment resuspension.
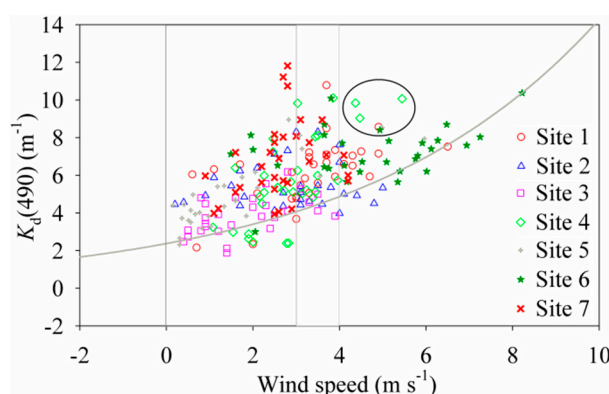

Figure 11. Scatterplot comparing wind speed and $K_d(490)$ in different sites. The regression line is at the floor level of $K_d(490)$ for different wind speeds.

5. Conclusions

The knowledge in respect of the short-term variation of the diffuse attenuation coefficient can help reveal its driving factors at the short time scales, such as wind speed. A semi-analytical algorithm of $K_d(490)$, which inserts an empirical model between the band-ratio ($R_{rs}(660)/R_{rs}(555)$) and $b_{bp}(660)$, was developed based on the in-situ measurement of R_{rs} and $K_d(490)$ for the high temporal-resolution of the GOCI satellite. The performance of the aforesaid semi-analytical algorithm for validation dataset shows that the RMSP and MAPE between the measured and the derived $K_d(490)$ are respectively 27.44% and 22.60 $\pm$ 15.57%. The RMSP and MAPE between the measured and the derived $K_d(490)$ are respectively 34.29% and 27.57 $\pm$ 20.56%, which indicated the feasibility of applying such algorithm in GOCI satellite images. The high temporal-resolution satellite data for monitoring the dynamic characteristics of $K_d(490)$ is necessary in the high dynamic-ratio lake. The comparison between GOCI- and MODIS-derived $K_d(490)$ manifested that GOCI-derived $K_d(490)$ can capture the spatial variation and the dynamic characteristics of $K_d(490)$ in a good manner. It's been found that wind is a primary driving factor in the spatial and temporal variation of $K_d(490)$, though its driving effect on $K_d(490)$ varied with the lacustrine morphometry (such as the effect in the center area of the lake is different from that in bays and the lake shore).

Author Contributions: Ling Yao principally conceived the idea for the study and was responsible for the design of the study, Changchun Huang was responsible for setting up experiments, completing the experiments and

retrieving data and he also wrote the initial draft of the manuscript. Ling Yao revised the paper. Both authors participated in some form in the concept, experimentation, writing and/or editing of this manuscript.

References

1. Kirk, J.T.O. Dependence of relationship between inherent and apparent optical properties of water on solar altitude. *Limnol. Oceanogr.* **1984**, *29*, 350–356. [CrossRef]

2. Preisendorfer, R.W. Hydrologic Optics, vol. 1. Introduction. Available online: http://udspace.udel.edu/handle/19716/1577 (accessed on 20 May 2017).

3. Lee, Z.P.; Darecki, M.; Carder, K.L.; Davis, C.; Stramski, D.; Rhea, W.J. Diffuse attenuation coefficient of downwelling irradiance: Anevaluation of remote sensing methods. *J. Geophys. Res.* **2005**, *110*. [CrossRef]

4. Lee, Z.; Hu, C.M.; Shang, S.; Du, K.; Lewis, M.; Arnone, R.; Brewin, R. Penetration of UV-Visible solar light in the global oceans: Insights from ocean color remote sensing. *J. Geophys. Res.* **2013**, *118*, 4241–4255. [CrossRef]

5. Shi, K.; Zhang, Y.L.; Liu, X.H.; Wang, M.Z.; Qin, B.Q. Remote sensing of diffuse attenuation coefficient of photosynthetically active radiation in Lake Taihu using MERIS data. *Remote Sens. Environ.* **2014**, *140*, 365–377. [CrossRef]

6. Song, K.S.; Ma, J.H.; Wen, Z.D.; Fang, C.; Shang, Y.X.; Zhao, Y.; Wang, M.; Du, J. Remote estimation of Kd(PAR) using MODIS and Landsat imagery for turbid inland waters in northeast China. *ISPRS J. Photogramm. Remote Sens.* **2017**, *123*, 159–172. [CrossRef]

7. Zhang, Y.L.; Liu, X.H.; Yin, Y.; Wang, M.Z.; Qin, B.Q. A simple optical model to estimate diffuse attenuation coefficient of photosynthetically active radiation in an extremely turbid lake from surface reflectance. *Opt. Express* **2012**, *20*, 20482–20493. [CrossRef] [PubMed]

8. Read, J.S.; Rose, K.C.; Winslow, L.A.; Read, E.K. A method for estimating the diffuse attenuation coefficient (KdPAR) from paired temperature sensors. *Limnol. Oceanogr. Methods* **2015**, *13*, 53–61. [CrossRef]

9. Wang, M.H.; Son, S.H.; Lawrence, W.; Harding, J. Retrieval of diffuse attenuation coefficient in the Chesapeake Bay and turbid ocean regions for satellite ocean color applications. *J. Geophys. Res.* **2009**, *114*. [CrossRef]

10. Wang, M.H.; Ahn, J.H.; Jiang, L.; Shi, W.; Son, S.H.; Park, Y.J.; Ryu, J.H. Ocean color products from the Korean Geostationary Ocean Color Imager (GOCI). *Opt. Express* **2013**, *21*, 3835–3849. [CrossRef] [PubMed]

11. Yu, X.L.; Salama, M.S.; Shen, F.; Verhoef, W. Retrieval of the diffuse attenuation coefficient from GOCI images using the 2SeaColor model: A case study in the Yangtze Estuary. *Remote Sens. Environ.* **2016**, *175*, 109–119. [CrossRef]

12. Zhang, T.L.; Fell, F. An empirical algorithm for determining the diffuse attenuation coefficient K_d in clear and turbid waters from spectral remote sensing reflectance. *Limnol. Oceanogr. Methods* **2007**, *5*, 457–462. [CrossRef]

13. Majozi, N.P.; Salama, M.S.; Bernard, S.; Harper, D.M.; Habte, M.G. Remote sensing of euphotic depth in shallow tropical inland waters of Lake Naivasha using MERIS data. *Remote Sens. Environ.* **2014**, *148*, 178–189. [CrossRef]

14. Zhang, G.; Stramski, D.; Reynolds, R.A. Evaluation of the QAA algorithm for estimating the inherent optical properties from remote sensing reflectance in Arctic waters. In Proceedings of the 2010 Ocean Sciences Meeting, Portland, OR, USA, 22–26 February 2010.

15. Chen, J.; Cui, T.W.; Tang, J.W.; Song, Q.J. Remote sensing of diffuse attenuation coefficient using MODIS imagery of turbid coastal waters: A case study in Bohai Sea. *Remote Sens. Environ.* **2014**, *140*, 78–93. [CrossRef]

16. Mueller, J.L. SeaWiFS algorithm for the diffuse attenuation coefficient, K(490), using water-leaving radiances at 490 and 555 nm. *SeaWiFS Postlaunch Calibration Valid. Anal.* **2000**, *3*, 24–27.

17. Wang, M.H.; Shi, W.; Tang, J.W. Water property monitoring and assessment for China's inland Lake Taihu from MODIS-Aqua measurements. *Remote Sens. Environ.* **2011**, *115*, 841–854. [CrossRef]

18. Saulquin, B.; Hamdi, A.; Gohin, F.; Populus, J.; Mangin, A.; d'Andona, O.F. Estimation of the diffuse attenuation coefficient K$_{dPAR}$ using MERIS and application to seabed habitat mapping. *Remote Sens. Environ.* **2015**, *128*, 224–233. [CrossRef]

19. Lee, Z.P.; Carder, K.L.; Robert, A.A. Deriving inherent optical properties from water color: A multiband quasi-analytical algorithm for optically deep waters. *Appl. Opt.* **2002**, *41*, 5755–5772. [CrossRef] [PubMed]

20. Doron, M.; Babin, M.; Mangin, A.; Hembise, O. Estimation of light penetration, and horizontal and vertical visibility in oceanic and coastal waters from surface reflectance. *J. Geophys. Res.* **2007**, *112*. [CrossRef]

21. Ma, R.H.; Pan, D.L.; Duan, H.T.; Song, Q.J. Absorption and scattering properties of water body in Taihu Lake, China: Backscattering. *Int. J. Remote Sens.* **2009**, *30*, 2321–2335. [CrossRef]

22. Huang, C.C.; Li, Y.M.; Yang, H.; Sun, D.Y.; Yu, Z.Y.; Zhang, Z.; Chen, X.; Xu, L.J. Detection of algal bloom and factors influencing its formation in Taihu Lake from 2000 to 2011 by MODIS. *Environ. Earth Sci.* **2014**, *71*, 3705–3714. [CrossRef]

23. Huang, C.C.; Shi, K.; Yang, H.; Li, Y.M.; Zhu, A.X.; Sun, D.Y.; Xu, L.J.; Zou, J.; Chen, X. Satellite observation of hourly dynamic characteristics of algae with Geostationary Ocean Color Imager (GOCI) data in Lake Taihu. *Remote Sens. Environ.* **2015**, *159*, 278–287. [CrossRef]

24. Guanter, L.; Ruiz-Verdú, A.; Odermatt, D.; Giardino, C.; Simis, S.; Estellés, V.; Heege, T.; Domínguez-Gómez, J.A.; Moreno, J. Atmospheric correction of ENVISAT/MERIS data over inland waters: Validation for European lakes. *Remote Sens. Environ.* **2010**, *114*, 467–480. [CrossRef]

25. Liu, G.; Li, Y.M.; Lv, H.; Wang, S.; Du, C.G.; Huang, C.C. An improved land target-based atmospheric correction method for Lake Taihu. *IEEE Sel. Top. Appl. Earth Obs. Remote Sens.* **2016**, *9*, 793–803. [CrossRef]

26. Budhiman, S.; Salama, M.S.; Vekerdy, Z.; Verhoef, W. Deriving optical properties of Mahakam Delta coastal waters, Indonesia using in situ measurements and ocean color model inversion. *ISPRS J. Photogramm. Remote Sens.* **2012**, *68*, 157–169. [CrossRef]

27. Huang, C.C.; Yao, L.; Huang, T.; Zhang, M.L.; Zhu, A.X.; Yang, H. Wind and rainfall regulation of the diffuse attenuation coefficient in large, shallow lakes from long-term MODIS observations using a semi-analytical model. *J. Geophys. Res. Atmos.* **2017**, *122*. [CrossRef]

28. Hu, C.M.; Lee, Z.P.; Ma, R.H.; Yu, K.; Li, D.Q.; Shang, S.L. Moderate Resolution Imaging Spectroradiometer (MODIS) observations of cyanobacteria blooms in Taihu Lake, China. *J. Geophys. Res. Oceans* **2010**, *115*, 216–263. [CrossRef]

29. Qin, B.; Hu, W.; Gao, G.; Luo, L.; Zhang, J. Dynamics of sediment resuspension and the conceptual schema of nutrient release in the large shallow Lake Taihu, China. *Chin. Sci. Bull.* **2004**, *49*, 54–64. [CrossRef]

30. Hawley, N. Response of the benthic nepheloid layer to near-inertial internal waves in southern Lake Michigan. *J. Geophys. Res.* **2004**, *109*, 249–260. [CrossRef]

31. Marti, C.L.; Imberger, J. Exchange between litto-ral and pelagic waters in a stratified lake due to wind-induced motions: Lake Kinneret, Israel. *Hydrobiologia* **2008**, *603*, 25–51. [CrossRef]

32. Valipour, R.; Boegman, L.; Bouffard, D.; Rao, Y.R. Sediment resuspension mechanisms and their contributions to high-turbidity events in a large lake. *Limnol. Oceanogr.* **2017**, *62*, 1045–1065. [CrossRef]

33. Cao, H.S.; Kong, F.X.; Luo, L.C.; Shi, X.L. Effects of wind and wind-induced waves on vertical phytoplankton distribution and surface blooms of Microcystis aeruginosa in Lake Taihu. *J. Freshw. Ecol.* **2016**, *21*, 231–238. [CrossRef]

34. Wynne, T.T.; Stumpf, R.P.; Tomlinson, M.C.; Dyble, J. Characterizing a cyanobacterial bloom in western Lake Erie using satellite imagery and meteorological data. *Limnol. Oceanogr.* **2010**, *55*, 2025–2036. [CrossRef]

35. Binding, C.E.; Greenberg, T.A.; Bukata, R.P. Time series analysis of algal blooms in Lake of the Woods using the MERIS maximum chlorophyll index. *J. Plankton Res.* **2011**, *33*, 1847–1852. [CrossRef]

36. Huang, C.C.; Yang, H.; Zhu, A.X.; Zhang, M.L.; Lü, H.; Huang, T.; Zou, J.; Li, Y.M. Evaluation of the Geostationary Ocean Color Imager (GOCI) to monitor the dynamic characteristics of suspension sediment in Taihu Lake. *Int. J. Remote Sens.* **2015**, *36*, 3859–3874. [CrossRef]